

Article

Oxygen Vacancy-Rich $\delta\text{-MnO}_2$ Cathode Materials for Highly Stable Zinc-Ion Batteries

Shilong Li and Xiang Wu * 

School of Materials Science and Engineering, Shenyang University of Technology, Shenyang 110870, China
* Correspondence: wuxiang05@sut.edu.cn

Abstract: As an emerging secondary battery system, aqueous zinc-ion batteries (AZIBs) show a broad application prospect in the fields of large-scale energy storage and wearable devices. Manganese-based cathode materials have been widely investigated by many researchers due to their high natural abundance, low toxicity, and multiple variable valence states. However, limited active sites, insufficient solvation, and reactivity kinetics of Mn^{2+} lead to the attenuation of their electrochemical performance. Herein, we introduce appropriate oxygen vacancies into the $\delta\text{-MnO}_2$ structure by modulating the annealing temperature. The obtained $\delta\text{-MnO}_2\text{-400}$ electrode provided 503 mAh/g capacity at 0.2 A/g and 99% capacity retention after 3000 times cycling at 1 A/g.

Keywords: zinc-ion battery; $\delta\text{-MnO}_2$; oxygen vacancy; annealing temperature; specific capacity

1. Introduction

Efficient and environmentally friendly energy storage technologies are becoming an important support for the development of modern society to address the problems of energy depletion and climate change [1,2]. Electrochemical energy storage shows tremendous potential for development, as the global energy transition and carbon reduction accelerate [3,4]. Lithium-ion batteries are widely used in electric vehicles, portable electronic devices, and other fields due to their high energy density, long life, environmental protection, and high performance [5]. Their use promotes green traveling, energy conservation, and emission reduction [6]. But they are at risk of thermal runaway when overcharged, over discharged, or subjected to physical damage, which can cause fires or even explosions. At the same time, the scarcity of lithium resources limits the sustainability of its large-scale application [7,8]. AZIBs have been a hot research topic in recent years and solve the existing problems at the present stage owing to their numerous advantages such as superior energy density, low cost and high safety [9,10]. The cathode materials are one of the major criteria for the performance evaluation of the battery [11,12]. They mainly include vanadium-based oxides [13], manganese-based oxides [14–16], Prussian blue analogs [17,18], polyanionic compounds [19], and quinone analogs [20]. In contrast, MnO_2 materials are favored for their high discharge platform, excellent electrochemical reactivity, and ease of preparation [21]. Also, their various polycrystalline structures, such as α , β , γ , ε , δ , λ , and other crystalline phase configurations confer different physical and chemical properties [22,23]. Among them, the $\delta\text{-MnO}_2$ material possesses a unique layered structure, which favors the formation of oxygen vacancies and electron transfer [24]. However, the actual specific capacity is inferior to the theoretical value and the capacity retention is poor at high current densities. This may be attributed to the fact that the repeated embedding/de-embedding of Zn^{2+} leads to the deformation or collapse of the electrode structure, which results in a rapid decrease in cycling stability. Moreover, the partial dissolution of Mn^{2+} increases the solution internal resistance and reduces the cell efficiency and lifetime. Therefore, the intrinsic capacity of the MnO_2 cathode is improved by expanding the layer spacing [25], constructing composites with conductive frameworks [26,27], and modifying the polycrystalline



Citation: Li, S.; Wu, X. Oxygen Vacancy-Rich $\delta\text{-MnO}_2$ Cathode Materials for Highly Stable Zinc-Ion Batteries. *Batteries* **2024**, *10*, 294. <https://doi.org/10.3390/batteries10080294>

Academic Editors: Jae-won Lee and Stefan Adams

Received: 9 July 2024

Revised: 18 August 2024

Accepted: 21 August 2024

Published: 22 August 2024



Copyright: © 2024 by the authors. Licensee MDPI, Basel, Switzerland. This article is an open access article distributed under the terms and conditions of the Creative Commons Attribution (CC BY) license (<https://creativecommons.org/licenses/by/4.0/>).

structure [28,29]. Despite some improvement, these advances have gradually reached a bottleneck and the products prepared still cannot address the demand for high-performance AZIBs [30].

The introduction of defect engineering provides new approaches to improve the electrochemical properties of transition metal oxides (TMOs) [31,32]. In different types of defects, oxygen vacancies play an essential role for local charge redistribution in TMOs. They can act as a shallow donor, changing the surface and geometry of the material, modulating the band gap and electron density to radically improve conductivity [33,34]. They also reduce the embedding energy barrier of Zn^{2+} in the cathode material and accelerate the charge transfer [35,36]. Furthermore, the generated vacancies form unsaturated coordination sites on the surface or inside the material. This contributes to the full contact between the active material and the electrolyte, effectively increasing the reaction rate and enhancing the charge storage capacity of the electrode [37,38]. For example, Cao et al. synthesized epsilon- MnO_2 nanosheets rich in oxygen vacancies, and the assembled battery delivered a capacity of 337 mAh/g at a current density of 0.1 A/g. The capacity retention rate is 85.9% after 1000 cycles [39]. Xu and co-workers et al. designed a $Zn//V-O-MnO_2@CNF$ battery that achieved a capacity of 135 mA h/g at a 1 A/g for 740 cycles [40]. Thus, oxygen vacancies contribute to the improvement of the reaction/diffusion kinetics of ions, providing excellent electrochemical properties for ZIBs.

In this work, we designed δ - MnO_2 -400 nanoflower structures using hydrothermal and annealing treatment. Appropriate oxygen vacancy concentrations were obtained by controlling different annealing temperatures. Compared to typical birnessite MnO_2 materials (with a specific capacity of 250–280 mA h/g, and a theoretical value of 308 mA h/g), we assembled $Zn//\delta$ - MnO_2 -400 cells offer a specific capacity of 503 mA h/g at 0.2 A/g. The capacity retention is 99% for 3000 cycles at 1 A/g current density. The introduction of oxygen defects in MnO_2 cathode materials provides an effective strategy for the development of high-performance AZIBs.

2. Experimental Section

2.1. Preparation of Materials

The chemicals used in the experiment were all of analytical grade (AR) and used directly without any purification. In total, 25 mL of 0.025 mol/L $MnSO_4$ and 25 mL of 0.15 mol/L $KMnO_4$ were mixed and stirred at room temperature for 30 min. Then, the mixture was transferred into an 80 mL Teflon-lined autoclave and kept at 160 °C for 12 h. The synthesized brown powder was washed with anhydrous ethanol and deionized (DI) water three times, respectively, and dried at 60 °C overnight. Finally, it was annealed in a muffle furnace at 2°/min for 2 h at 300 °C, 400 °C, and 500 °C. The final obtained samples were named δ - MnO_2 , δ - MnO_2 -300, δ - MnO_2 -400, and δ - MnO_2 -500, respectively.

2.2. Morphology and Structure Characterization

The morphologies of the samples were observed using a scanning electron microscope (SEM, Tescan mira3Zeiss sigma500) and a high-resolution transmission electron microscope (HRTEM, FEI Tecnai G2 F30JEOL-2100F). The crystal structure and chemical bonding were characterized using X-ray diffraction (XRD, Shimadzu-7000, Cu K α radiation, $k = 0.1541$ nm), an X-ray Photoelectron Spectrometer (XPS, Thermo Scientific Escalab 250 Xi) and Electron Paramagnetic Resonance (EPR, Bruker EMX plus). Specific surface area, pore size, and elemental distribution were determined using the N_2 adsorption-desorption isotherm method (BET, JWGB-T200) and energy dispersive spectroscopy (EDS), respectively.

2.3. Electrochemical Characterization

The active substance, super p, and polyfluoroethylene were ground with a mass ratio (7:2:1) and an appropriate amount of N-methyl-2 pyrrolidone (NMP) was added to form a slurry. They were then evenly coated on carbon paper and kept in a vacuum oven at 60 °C for 12 h. Type 2032 cells were assembled at room temperature by the obtained samples, glass

fiber separator, electrolyte ($2\text{ M ZnSO}_4 + 0.2\text{ M MnSO}_4$), and zinc foil. The average mass of the cathode material was $1.05\text{--}1.5\text{ mg}$. Cyclic voltammetry (CV) and electrochemical impedance spectroscopy (EIS) were tested in an electrochemical workstation (CHI660E). Cycling, multiplier performance, and the galvanostatic charge/discharge (GCD) curves were tested on the Neware (CT-4008 T) system.

3. Results and Discussion

We firstly characterized the crystal structure of the samples using XRD. It is noteworthy from Figure 1a that the annealing temperature can affect the crystallographic orientation of MnO_2 materials. The diffraction peaks of the $\delta\text{-MnO}_2\text{-300}$ and $\delta\text{-MnO}_2\text{-400}$ powders at 12.1° , 24.6° , 36.9° , and 66.1° correspond to the (001), (002), (11-1), and (114) planes, respectively. They can be indexed as MnO_2 phases with a birnessite structure (JCPDs no. 13-0105), and no other peaks are found, which proves their high purity. The peaks at the (001) and (11-1) crystal planes gradually broaden with increasing temperature, indicating that the generated vacancy defects induced lattice distortion [41,42]. In addition, the structure is destroyed due to its poor thermal stability and a phase transition occurs at 500° . Its diffraction peaks match well with the MnO_2 phase (JCPDs no. 72-1982). Figure 1b shows the N_2 isothermal curves and pore size distributions of the four samples. The specific surface area of $\delta\text{-MnO}_2\text{-400}$ is $63\text{ m}^2/\text{g}$, which is larger than the other three samples ($\delta\text{-MnO}_2$: $23\text{ m}^2/\text{g}$; $\delta\text{-MnO}_2\text{-300}$: $53\text{ m}^2/\text{g}$; and $\delta\text{-MnO}_2\text{-500}$: $17\text{ m}^2/\text{g}$). This can be attributed to the introduction of oxygen vacancies. This mitigates the volume change during the redox process while providing sufficient active sites. Their pore sizes are 4.6 nm , 4.3 nm , 3.2 nm , and 2.8 nm , respectively. The mesoporous structure facilitates the penetration of the electrolyte and effectively accelerates the rapid migration of Zn^{2+} , thus allowing the active material to be fully utilized. However, the appearance of a new phase may occupy the space that originally belongs to the main material, leading to the reduction in the voids between the nanosheets.

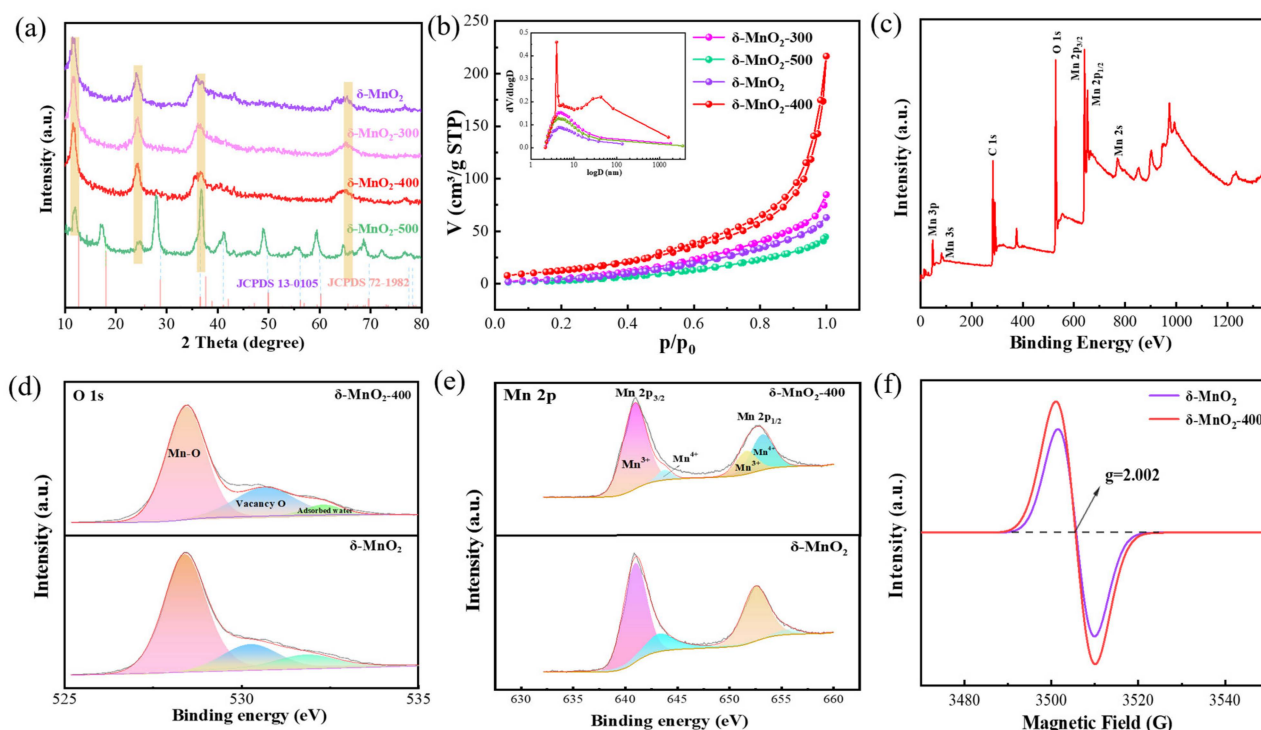


Figure 1. Structure characterization: (a) XRD patterns of four samples; (b) N_2 isotherms and pore size; (c–e) XPS survey spectra of O 1s and Mn 2p; (f) EPR.

Then, XPS was used to study the chemical composition and valence distribution of the $\delta\text{-MnO}_2$ and $\delta\text{-MnO}_2\text{-400}$ samples. The signal peaks of Mn 2p, Mn 3p, Mn 3s, Mn 2s,

and O 1s can be found in the survey spectra (Figure 1c). In Figure 1d, the peaks located at 528.28 eV, 530.98 eV, and 532.43 eV can be assigned to Mn-O bonds, oxygen vacancies, and adsorbed oxygen [43]. It can be obviously observed that the peak intensity of the δ -MnO₂-400 sample is stronger than that of the pristine sample. The results confirm an increase in the vacancy concentration of the samples after annealing treatment, which is in agreement with previous reports [44]. From Figure 1e, Mn 2p_{3/2} and Mn 2p_{1/2} are located at 640.88 eV and 652.98 eV, with a spin difference of 12.1 eV, which is consistent with the characteristics of the MnO₂ material [45]. In the Mn2p_{1/2} orbital, the integral area of Mn³⁺/Mn⁴⁺ gradually changes in order to balance the produced oxygen vacancies. In addition, EPR can further confirm the increase in the concentration of vacancies, as shown in Figure 1f. Because the electrons are bound by vacancy, there is an electron spin resonance (ESR) signal at $g = 2.002$ [46]. The ESR intensity of the δ -MnO₂-400 sample is higher than that of δ -MnO₂, indicating sufficient oxygen vacancy, which is consistent with the XPS results.

The morphology of the four samples was observed using SEM. They are all microspheres consisting of smooth and intersecting nanosheets (Figure 2a–d). This unique structure ensures that the nanosheets possess sufficient gaps between them to provide channels for the transport of ions and accelerate the reaction rate. It can be observed that some nanorods are interspersed between the microspheres owing to the high annealing temperature. They may not only clog the pores of the matter, but also promote the agglomeration phenomenon. This is the main reason for the small specific surface area of the δ -MnO₂-500 material. At the same time, the creation of new phases changes the chemistry of the material and affects its electrochemical properties. This will be discussed in detail in the next section. In addition, the microstructures of the δ -MnO₂-400 and δ -MnO₂-500 powders were investigated using HRTEM, respectively, as shown in Figure 2e–h. The interplanar spacings of 0.262 nm and 0.244 nm can be indexed to the (11-1) and (510) crystal planes, respectively, and can be calculated from line profiles. As seen the EDS (Figure 2i), the Mn and O elements are uniformly distributed on the surface.

In Figure 3a, some button cells are assembled at room temperature in order to investigate the effect of annealing temperatures on the electrochemical properties of the δ -MnO₂ electrode. Figure 3b shows the CV of the δ -MnO₂-400 cathode from the first to third circles at 0.2 mV/s in the voltage range of 0.8–2 V. The two pairs of redox peaks prove that the reaction process is a two-step process, which refers to the insertion/extraction of H⁺ and Zn²⁺ ions. Also, compared with other electrodes, δ -MnO₂-400 possesses higher current intensity and lower polarization, demonstrating higher chemical activity and superior electrochemical performance. Figure 3c shows the CV of the δ -MnO₂-400 cathode from the first to third circles. The overlap of the curve shapes indicates that the reaction is highly reversible. Meanwhile, it can be observed that there are two discharge platforms located at 1.39 V and 1.22 V in the GCD curves. The rate performance is an important criterion for evaluating ZIBs. As can be seen from Figure 3d–f, the specific capacity of the δ -MnO₂-400 batteries can reach 500, 308, 154, 83, 51, and 29 mAh/g at 0.2, 0.5, 1, 2, 3, and 5 A/g, respectively. When the current density is restored to 0.2 A/g, the capacity retention rate is 81.7%. The GCD curve shows that the capacity decreases with the increase in current density. In addition, the cell retains a capacity of 417 mAh/g after 100 cycles at 0.2 A/g (Figure 3g). Significantly, it maintains 99% capacity retention and 100% coulombic efficiency after 3000 cycles, as shown in Figure 3h. Table 1 lists the various data of different types of batteries [15,47–57]. The above results demonstrate the excellent cycling stability of the prepared δ -MnO₂-400 cathodes.

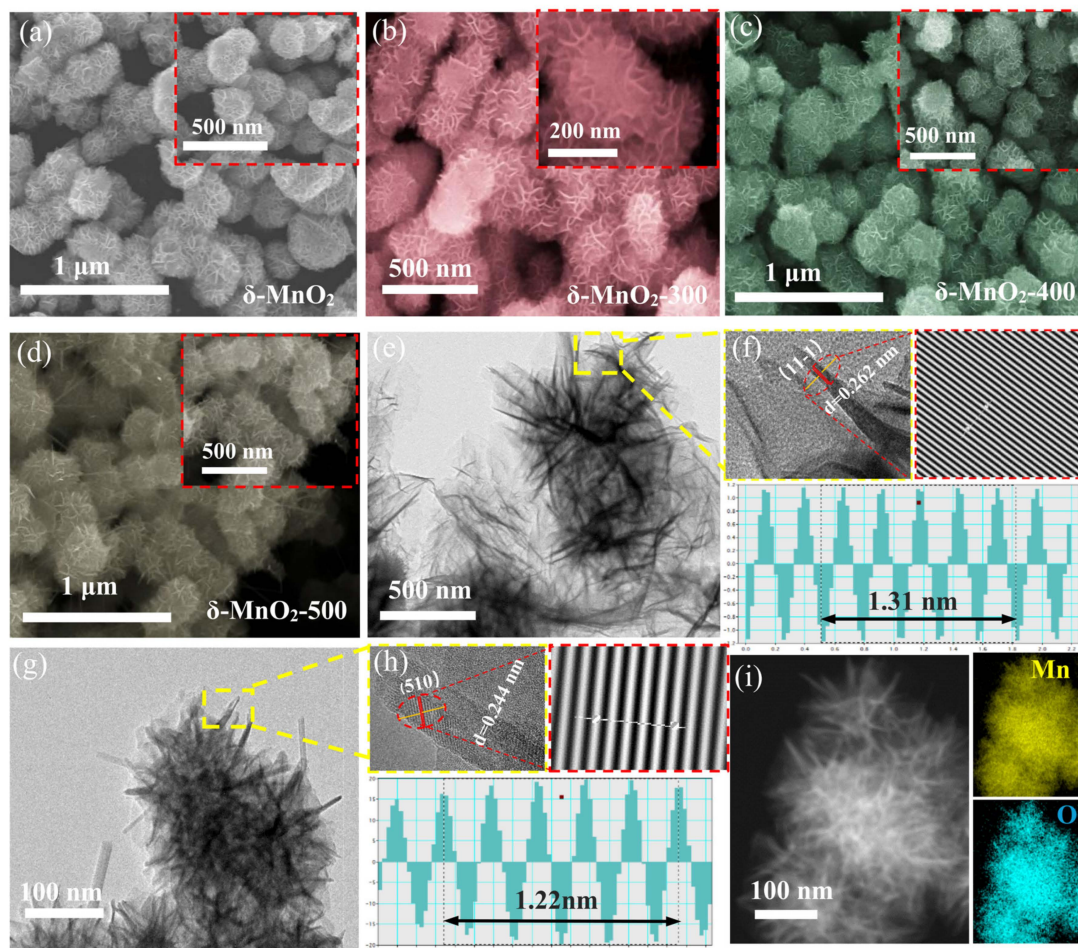


Figure 2. Morphology characterization: (a–d) SEM images of four powders; (e–h) TEM and HRTEM images of $\delta\text{-MnO}_2\text{-}400$ and $\delta\text{-MnO}_2\text{-}500$; (i) EDS.

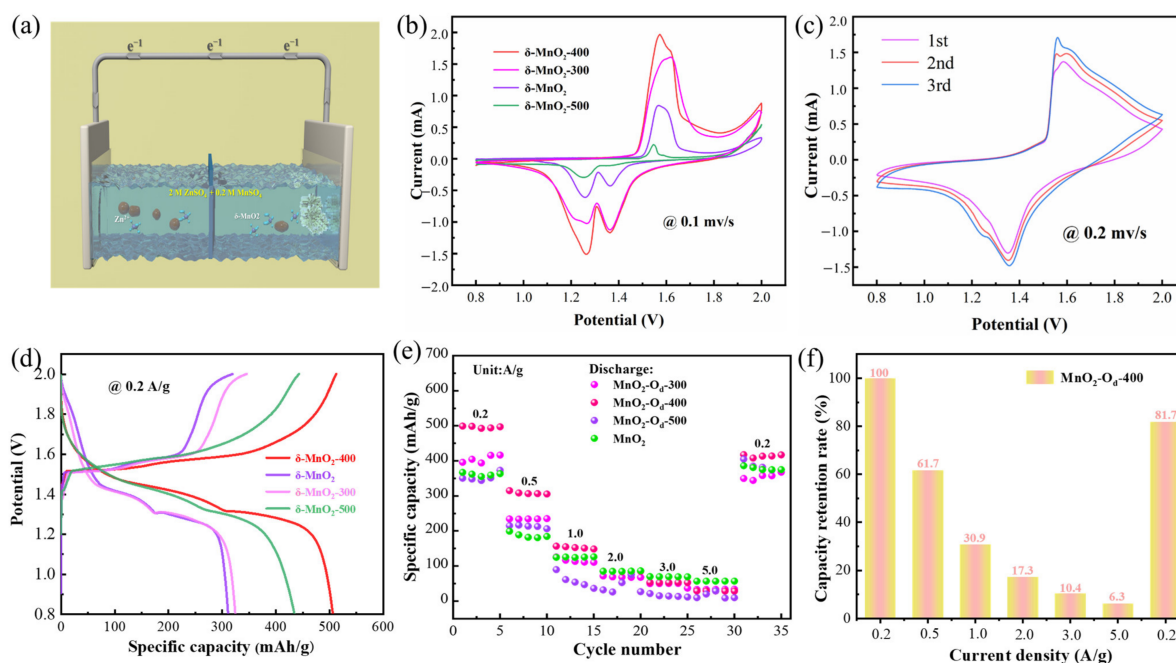


Figure 3. Cont.

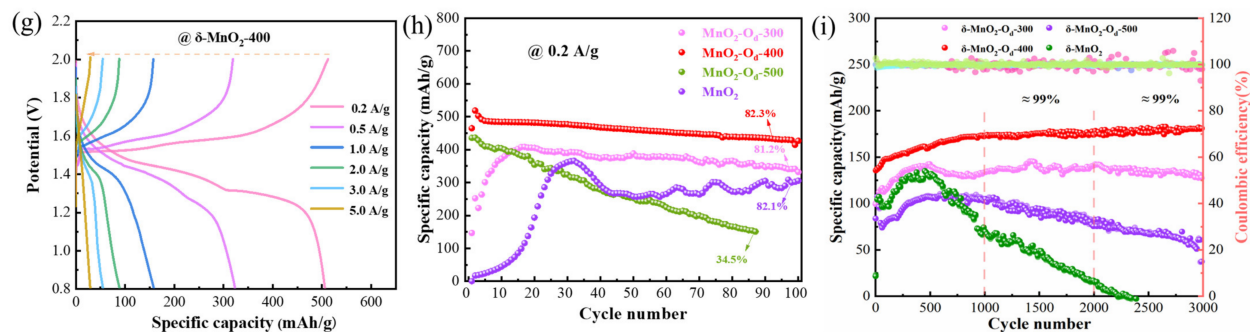


Figure 3. Electrochemical performance: (a) The ZIB structure of $\delta\text{-MnO}_2\text{-}X$; (b) CV curves of $\delta\text{-MnO}_2\text{-}X$; (c) CV of $\delta\text{-MnO}_2\text{-}400$ at 0.2 mV/s; (d) GCD curves of four electrodes; (e) rate capability; (f) capacity retention rate of $\delta\text{-MnO}_2\text{-}400$; (g) GCD curves of $\delta\text{-MnO}_2\text{-}400$; (h,i) cycling performance at 1.0 A/g.

Table 1. Initial capacity of various cathode materials.

Materials	Potential Window (V)	Current Density (A/g)	Specific Capacity (mAh/g)	Cycling Stability	Energy Density (W h/kg)	Ref.
$\text{O}_d\text{-HVO}$	0.2–1.6	0.2/2.0	337/334	85%	228	[47]
$\gamma\text{-MnO}_2$	0.8–1.8	0.05	285	-	-	[48]
$\beta\text{-MnO}_2$	1.0–1.8	0.1	100	-	-	[49]
Na^+ doping VO_2	0.2–1.6	0.2/12	345/156	$\approx 95\%$	278	[50]
ZnO-QDs-VN	0.4–1.6	0.1	384.1	$\approx 54\%$	209	[51]
$\alpha\text{-MnO}_2$	1.0–1.85	C/3/5C	285/100	92%	-	[15]
Od-MnO_2	1.0–1.8	0.2	345	94%	235	[52]
$\text{MnO}_2@\text{PANI}$	1.0–1.85	0.2	342	82%	199.5	[53]
$\text{K-}\delta\text{-MnO}_2$	1.0–1.8	0.1/2.0	270.3/63.9	$\approx 46\%$	108.1	[54]
S-MnO_2	0.8–1.8	0.2/2.0	324/205	$\approx 77\%$	194.4	[55]
V-doped MnO_2	1.0–1.8	0.066	266	-	-	[56]
$\delta\text{-MnO}_2$ NDS	1.0–1.9	0.1/2.0	335/125	86.2%	233	[57]
$\delta\text{-MnO}_2\text{-}400$	0.8–2.0	0.2/1.0	503/154	99%	300	This work

We further investigated $\delta\text{-MnO}_2\text{-}400$'s electrochemical kinetics and energy storage mechanism by utilizing CV, GITT, and EIS. Figure 4a shows the CV curves at 0.1–0.5 mV/s, with the redox peak shift with the sweep speed increasing. The peak intensities located at 1.21 V and 1.67 V are gradually smooth. This is due to the inability of reactants on the electrode surface to diffuse in time or the formation of intermediates becoming less obvious, resulting in peak merging. In addition, the peak current (i) and sweep rate (v) can be defined by the following equation [58]:

$$i = av^b \quad (1)$$

where a and b are adjustable parameters, where the value of b can quantify the contribution of surface and diffusion control, as shown in Figure 4b,c. After fitting, the four b values of the $\delta\text{-MnO}_2\text{-}400$ electrode are 0.63 (peak 1), 0.69 (peak 2), 0.75 (peak 3), and 0.77 (peak 4). This suggests that capacitance control and diffusion synergistically dominate the charge storage [59]. In addition, the contribution of the pseudo-capacitance ($k_1 v$) and the diffusion component ($k_2 v^{1/2}$) can be expressed by equation [60]:

$$i = k_1 v + k_2 v^{1/2} \quad (2)$$

where i is the current at a fixed potential. Capacitive contribution increases from the original 44.4% to 72.6% with sweep speed, demonstrating its excellent electrochemical kinetics. The Zn^{2+} diffusion coefficients (D_{Zn}^{2+}) of the samples are then estimated using

the galvanostatic intermittent titration technique (GITT) (Figure 4d). It is calculated using the following formula [61]:

$$D = \frac{4L^2}{\pi\tau} \left(\frac{\Delta E_s}{\Delta E_t} \right)^2 \quad (3)$$

where τ is the relaxation time; ΔE_s is the pulse-induced voltage change and ΔE_t is the voltage change for constant current charging (discharging). The discharge process is divided into two regions; the first region (platform I) corresponds mainly to the embedding of H^+ , while the second region (platform II) is dominated by the embedding of Zn^{2+} . The ionic diffusion coefficients of platform I are between 10^{-8} and $10^{-6} \text{ cm}^2/\text{s}$, whereas those of platform II are about $10^{-10} \text{ cm}^2/\text{s}$. This is attributed to the large difference in the radii of H^+ and Zn^{2+} , with the H^+ ionic diffusion coefficient being two orders of magnitude higher than that of Zn^{2+} . This is in accordance with the above studies on the kinetics of redox reactions at the MnO_2 electrode. The $D_{Zn^{2+}}$ of $\delta\text{-MnO}_2\text{-400}$ ($10^{-6}\text{--}10^{-8} \text{ cm}^2/\text{s}$) is significantly higher than that of the other obtained cathodes, demonstrating its excellent kinetics. Compared to the other three electrodes, $\delta\text{-MnO}_2\text{-400}$ shows the longest discharge time, representing more time for Zn^{2+} to diffuse inside the electrode material during the relaxation phase (the phase where no current passes through). This helps the ions to achieve a more uniform distribution within the active material, thus reducing the phenomenon of concentrated polarization. Meanwhile, the proper oxygen vacancies play an important role in facilitating the transport of Zn^{2+} .

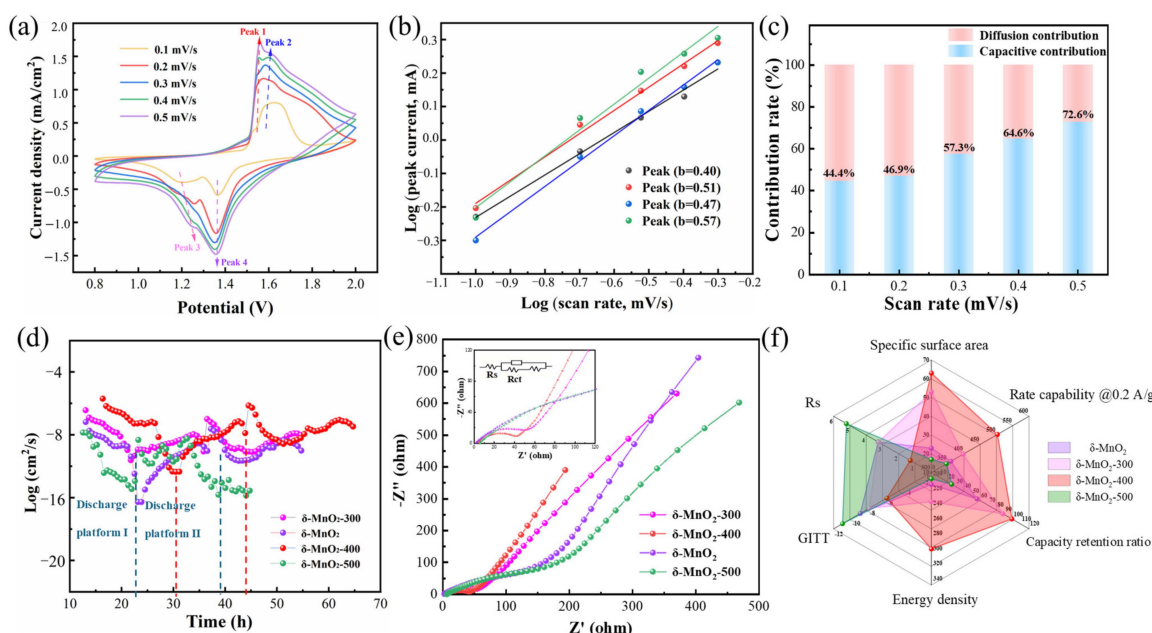


Figure 4. Reaction kinetics: (a) CV curves of $\delta\text{-MnO}_2\text{-400}$ at 0.1–0.5 mV/s; (b) $\log(i)$ versus $\log(v)$; (c) capacitive contribution ratios; (d) GITT; (e) EIS; (f) radar chart.

As shown in Figure 4e, we further studied the EIS of the $Zn / \delta\text{-MnO}_2\text{-X}$ cells in the range of 100 kHz–0.01 Hz. In the high-frequency region, the diameter of the semicircle in the curve is the charge transfer resistance (R_{ct}) between the electrode and the electrolyte. Its size is proportional to the resistance. In the low-frequency region, the slope of the straight line (Z_w) represents the degree of ion diffusion. In addition, the intercept between the straight line and the X-axis is the series resistance (R_s) (the solution internal resistance). In contrast, the $\delta\text{-MnO}_2\text{-400}$ electrode show smaller R_s ($\delta\text{-MnO}_2$: 3.248; $\delta\text{-MnO}_2\text{-300}$: 3.267; $\delta\text{-MnO}_2\text{-400}$: 1.292; $\delta\text{-MnO}_2\text{-500}$: 5.215) and R_{ct} (98; 42; 29; 104) and higher slopes. This indicates a rapid and effective ion transport diffusion process. For the electrode materials, the energy density and power density are calculated using the following equations (Equations (4) and (5)):

$$E = QU/2m \quad (4)$$

$$P = iU/2m \quad (5)$$

where E (W h/kg) is the energy density and P is the power density (kW/kg). Q (A h), V (V), i (A), and m (kg) denote the discharge capacity of cathode, the operating potential, the discharge current, and the mass load. The energy density of the Zn// δ -MnO₂-400 cell is calculated to be 300 Wh/kg at a power density of 60 W/kg. We used radar charts in order to compare the performance of different electrodes (Figure 4f). Taken together, the δ -MnO₂-400 cathode possesses excellent reaction kinetics and rate performance.

In order to further explore the energy storage mechanism, we studied the structure of δ -MnO₂-400 samples at specific charging/discharging states using ex situ XRD and XPS. Figure 5a,b show the XRD patterns in different states. During the first cycle of the discharge, the (001) plane shifts 0.5° from 12.16° to the left, suggesting that Zn²⁺ is successfully inserted into the host structure. In the subsequent reaction process, some additional peaks are generated at 11.58° and 38.94°, which can be indexed to the zinc sulfate hydrate ($Zn_4SO_4(OH)_6 \cdot 4H_2O$, ZSH, PDF: 44-0673) phases [62]. Also, the ZnMn₂O₄ (ZMO, PDF: 77-0470) phase is detected. When charged to 2.0 V, the (001) crystalline peak returns to 12.14°, which can be attributed to the shuttling effect of Zn²⁺. In addition, the new peaks gradually disappear as the reaction proceeds again, demonstrating the high reversibility of the δ -MnO₂-400 sample. Then, we studied the XPS at different voltages of the electrodes in order to verify the phase transition process. The Mn 2p spectra are convoluted into three peaks, situated at 638.78, 641.08, and 643.68 eV, corresponding to Mn²⁺, Mn³⁺, and Mn⁴⁺, respectively (Figure 5c). The presence of Mn²⁺ may be caused by the embedding of Zn²⁺ resulting in the reduction in part of the Mn³⁺ to Mn²⁺ [63]. It also can be observed that the intensity of the Mn³⁺ and Mn⁴⁺ peaks diminishes at complete discharge to 0.8 V. Figure 5d shows the Zn 2p spectra with characteristic peaks at 1020.98 eV and 1044.08 eV. The decrease in peak intensity compared to the discharge state is due to the precipitation of Zn²⁺ and the decomposition of ZSH.

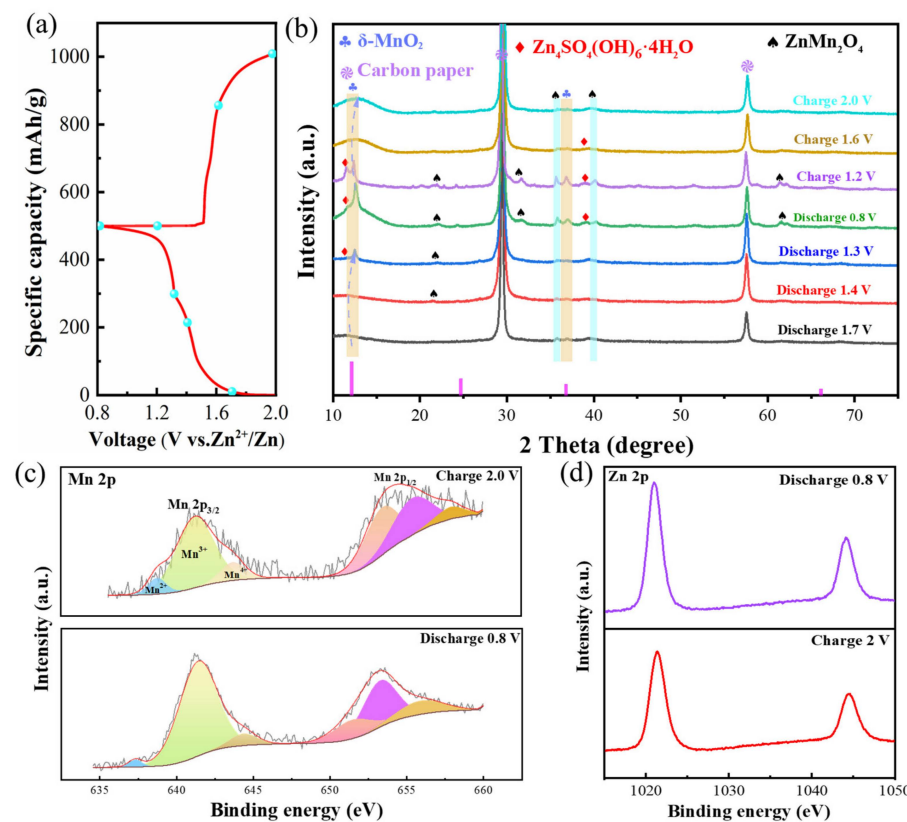


Figure 5. (a,b) ex situ XRD patterns; (c) Mn 2p; (d) Zn 2p.

4. Conclusions

In summary, we prepared several Mn-based electrode materials for zinc-ion batteries. The introduction of appropriate oxygen vacancies accelerated the transport rates of Zn^{2+} and H^+ and promoted the electrochemical reactions. At the same time, it improved the charge transfer and structural stability of the material. These advantages lead to a high specific capacity, long cycle life, and high energy density of the assembled $Zn//\delta\text{-MnO}_2\text{-}400$ cells. This study provides potential high-performance cathode materials for next-generation ZIBs. Also, it puts forward an effective vacancy modulation strategy to design future electrode materials for portable micro-/nano-devices.

Author Contributions: Conceptualization, S.L. and X.W.; Software, S.L.; Validation, S.L.; Formal analysis, S.L. and X.W.; Investigation, S.L.; Resources, X.W.; Data curation, S.L. and X.W.; Writing—original draft, S.L.; Writing—review & editing, X.W.; Project administration, X.W.; Funding acquisition, X.W. All authors have read and agreed to the published version of the manuscript.

Funding: This research received no external funding.

Data Availability Statement: Data are contained within the article.

Conflicts of Interest: The authors declare no conflicts of interest.

References

1. Zhang, J.N.; Xiao, J.F.; Chen, X.F.; Liang, X.M.; Fan, L.Y.; Ye, D.Q. Allowance and allocation of industrial volatile organic compounds emission in China for year 2020 and 2030. *J. Environ. Sci.* **2018**, *69*, 155–165. [[CrossRef](#)] [[PubMed](#)]
2. Liu, Y.; Liu, Y.; Wu, X.; Cho, Y.R. A facile carbon modification avenue to construct highly stable V_2O_5 electrode for aqueous zinc ion batteries. *ACS Sustain. Chem. Eng.* **2023**, *11*, 13298–13305. [[CrossRef](#)]
3. Fitz, O.; Ingenhoven, S.; Bischoff, C.; Gentischer, H.; Birke, K.P.; Saracsan, D.; Biro, D. Comparison of aqueous-and non-aqueous-based binder polymers and the mixing ratios for $Zn//\text{MnO}_2$ batteries with mildly acidic aqueous electrolytes. *Batteries* **2021**, *7*, 40. [[CrossRef](#)]
4. Zhang, L.; Yang, S.H.; Fu, W.Q.; Cui, Y.W.; Wang, J.Q.; Zhao, D.G.; Yang, C.; Wang, X.T.; Cao, B.Q. Plasma-induced $\varepsilon\text{-MnO}_2$ based aqueous zinc-ion batteries and their dissolution-deposition mechanism. *J. Mater. Sci. Technol.* **2022**, *127*, 206–213. [[CrossRef](#)]
5. Li, S.L.; Zhao, M.; Zhang, D.D.; Wu, X. High-capacity aqueous Zn/MnO_2 batteries: A clue of K ion pre-intercalation. *Cryst. Growth Des.* **2023**, *23*, 8156–8162. [[CrossRef](#)]
6. Wang, T.T.; Li, C.P.; Xie, X.S.; Lu, B.G.; He, Z.X.; Liang, S.Q.; Zhou, J. Anode materials for aqueous zinc ion batteries: Mechanisms, properties, and perspectives. *ACS Nano* **2020**, *14*, 16321–16347. [[CrossRef](#)]
7. Liu, Y.; Umar, A.; Wu, X. Metal-organic framework derived porous cathode materials for hybrid zinc ion capacitor. *Rare Met.* **2022**, *41*, 2985–2991. [[CrossRef](#)]
8. Durena, R.; Zukuls, A. A Short Review: Comparison of Zinc-Manganese dioxide batteries with different pH aqueous electrolytes. *Batteries* **2023**, *9*, 311. [[CrossRef](#)]
9. Liu, Y.; Wu, X. Review of vanadium-based electrode materials for rechargeable aqueous zinc ion batteries. *J. Energy Chem.* **2021**, *56*, 223–237. [[CrossRef](#)]
10. Chen, L.N.; An, Q.Y.; Mai, L.Q. Recent advances and prospects of cathode materials for rechargeable aqueous zinc-ion batteries. *Adv. Mater. Interfaces* **2019**, *6*, 1900387. [[CrossRef](#)]
11. Zhang, J.J.; Wu, X. Dual-ion carrier storage through Mg^{2+} addition for high-energy and long-life zinc-ion hybrid capacitor. *Int. J. Min. Met. Mater.* **2024**, *31*, 179–185. [[CrossRef](#)]
12. Yan, M.Y.; He, P.; Chen, Y.; Wang, S.Y.; Wei, Q.L.; Zhao, K.N.; Xu, X.; An, Q.Y.; Shuang, Y.; Shao, Y.Y.; et al. Water-lubricated intercalation in $V_2O_5\cdot nH_2O$ for high-capacity and high-rate aqueous rechargeable zinc batteries. *Adv. Mater.* **2018**, *30*, 1703725. [[CrossRef](#)] [[PubMed](#)]
13. Liu, Y.; Liu, Y.; Wu, X. Defect engineering of vanadium-based electrode materials for zinc ion battery. *Chinese Chem. Lett.* **2023**, *34*, 107839. [[CrossRef](#)]
14. Zhang, N.; Cheng, F.Y.; Liu, Y.C.; Zhao, Q.; Lei, K.X.; Chen, C.C.; Liu, X.S.; Chen, J. Cation-deficient spinel $ZnMn_2O_4$ cathode in $Zn(CF_3SO_3)_2$ electrolyte for rechargeable aqueous Zn-ion battery. *J. Am. Chem. Soc.* **2016**, *138*, 12894–12901. [[CrossRef](#)]
15. Pan, H.L.; Shao, Y.Y.; Yan, P.F.; Cheng, Y.W.; Han, K.S.; Nie, Z.M.; Wang, C.M.; Yang, J.H.; Li, X.L.; Bhattacharya, P.; et al. Reversible aqueous zinc/manganese oxide energy storage from conversion reactions. *Nat. Energy* **2016**, *1*, 16039. [[CrossRef](#)]
16. Sun, W.; Wang, F.; Hou, S.Y.; Yang, C.Y.; Fan, X.L.; Ma, Z.H.; Han, F.D.; Hu, R.D.; Zhu, M.; Wang, C.S. Zn/MnO_2 battery chemistry with H^+ and Zn^{2+} co-insertion. *J. Am. Chem. Soc.* **2017**, *139*, 9775–9778. [[CrossRef](#)]
17. Zhang, L.Y.; Chen, L.; Zhou, X.F.; Liu, Z.P. Towards high-voltage aqueous metal-ion batteries beyond 1.5 V: The zinc/zinc hexacyanoferrate system. *Adv. Energy Mater.* **2015**, *5*, 1400930. [[CrossRef](#)]
18. Trócoli, R.; Mantia, F. An aqueous zinc-ion battery based on copper hexacyanoferrate. *ChemSusChem* **2015**, *8*, 481–485. [[CrossRef](#)]

19. Wang, K.H.; Shangguan, M.L.; Zhao, Y.B.; Tian, H.R.; Wang, F.; Yuan, J.L.; Lan, X. Flexible and stable n-isopropylacrylamide/sodium alginate gel electrolytes for aqueous Zn-MnO₂ batteries. *Batteries* **2023**, *9*, 426. [[CrossRef](#)]
20. Zhao, Q.; Huang, W.W.; Luo, Z.Q.; Liu, L.J.; Lu, Y.; Li, Y.X.; Ma, H.; Chen, J. High-capacity aqueous zinc batteries using sustainable quinone electrodes. *Sci. Adv.* **2018**, *4*, 1761. [[CrossRef](#)]
21. Wen, S.; Gu, X.; Ding, X.W.; Dai, P.C.; Zhang, D.J.; Li, L.J.; Liu, D.D.; Zhao, X.B.; Yang, J. Boosting fast and stable alkali metal ion storage by synergistic engineering of oxygen vacancy and amorphous structure. *Adv. Funct. Mater.* **2021**, *32*, 2106751. [[CrossRef](#)]
22. Xie, H.X.; Cui, J.X.; Yao, Z.; Ding, X.K.; Zhang, Z.H.; Luo, D.; Lin, Z. Revealing the role of spinel phase on Li-rich layered oxides: A review. *Chem. Eng. J.* **2022**, *427*, 131978. [[CrossRef](#)]
23. Luo, H.; Wang, B.; Jian, J.H.; Wu, F.D.; Peng, L.; Wang, D.L. Stress-release design for high-capacity and long-time lifespan aqueous zinc-ion batteries. *Mater. Today Energy* **2021**, *21*, 100799. [[CrossRef](#)]
24. Yadav, P.; Putro, D.; Kim, J.; Rai, A.K. Pom-pom flower-like morphology of δ-MnO₂ with superior electrochemical performances for rechargeable aqueous zinc ion batteries. *Batteries* **2023**, *9*, 133. [[CrossRef](#)]
25. Liu, Y.; Liu, Y.; Wu, X.; Cho, Y.R. Enhanced electrochemical performance of Zn/VO_x batteries by a carbon-encapsulation strategy. *ACS Appl. Mater. Interfaces* **2022**, *14*, 11654–11662. [[CrossRef](#)]
26. Cao, Z.W.; Zhang, H.; Song, B.; Xiong, D.Y.; Tao, S.S.; Deng, W.T.; Hu, J.G.; Hou, H.S.; Zou, G.Q.; Ji, X.B. Angstromlevel ionic sieve 2D-MOF membrane for high power aqueous zinc anode. *Adv. Funct. Mater.* **2023**, *33*, 2300339. [[CrossRef](#)]
27. Liu, C.; Deng, L.J.; Li, X.Z.; Wu, T.; Zhang, W.J.; Cui, H.S.; Yang, H. Metal–organic frameworks for solid-state electrolytes: A mini review. *Electrochim. Commun.* **2023**, *150*, 107491. [[CrossRef](#)]
28. Wei, C.G.; Xu, C.J.; Li, B.H.; Du, H.D.; Kang, F.Y. Preparation and characterization of manganese dioxides with nano-sized tunnel structures for zinc ion storage. *J. Phys. Chem. Solids* **2012**, *73*, 1487–1491. [[CrossRef](#)]
29. Alfaruqi, M.H.; Islam, S.; Putro, D.Y.; Mathew, V.; Kim, S.; Jo, J.; Kim, S.; Sun, Y.K.; Kim, K.; Kim, J. Structural transformation and electrochemical study of layered MnO₂ in rechargeable aqueous zinc-ion battery. *Electrochim. Acta* **2018**, *276*, 1–11. [[CrossRef](#)]
30. Huang, J.H.; Wang, Z.; Hou, M.Y.; Dong, X.L.; Liu, Y.; Wang, Y.G.; Xia, Y.Y. Polyaniline-intercalated manganese dioxide nanolayers as a high-performance cathode material for an aqueous zinc-ion battery. *Nat. Commun.* **2018**, *9*, 2906. [[CrossRef](#)]
31. Jiang, J.; Xu, T.; Lu, J.P.; Sun, L.T.; Ni, Z.H. Defect engineering in 2D materials: Precise manipulation and improved functionalities. *Research* **2019**, *2019*, 4641739. [[CrossRef](#)] [[PubMed](#)]
32. Xie, C.; Yan, D.F.; Chen, W.; Zou, Y.Q.; Chen, R.; Zang, S.Q.; Wang, Y.Y.; Yao, X.D.; Wang, Y.Y.; Yao, X.D.; et al. Insight into the design of defect electrocatalysts: From electronic structure to adsorption energy. *Mater. Today* **2019**, *31*, 47–68. [[CrossRef](#)]
33. Zhao, J.; Cheng, H.; Zhang, Z.H.; Liu, Y.; Song, J.N.; Liu, T.; He, Y.N.; Meng, A.L.; Sun, C.L.; Hu, M.; et al. The semicoherent interface and vacancy engineering for constructing Ni(Co)Se₂@Co(Ni)Se₂ heterojunction as ultrahigh-rate battery-type supercapacitor cathode. *Adv. Funct. Mater.* **2022**, *32*, 2202063. [[CrossRef](#)]
34. Zheng, Y.J.; Yao, Z.G.; Shadike, Z.; Lei, M.; Liu, J.J.; Li, C.L. Defect concentration-mediated T-Nb₂O₅ anodes for durable and fast charging Li-ion batteries. *Adv. Funct. Mater.* **2022**, *32*, 2107060. [[CrossRef](#)]
35. Zhao, Y.X.; Chang, C.; Teng, F.; Zhao, Y.F.; Chen, G.B.; Shi, R.; Waterhouse, G.; Huang, W.F.; Zhang, T.R. Defect-engineered ultrathin δ-MnO₂ nanosheet arrays as bifunctional electrodes for efficient overall water splitting. *Adv. Energy Mater.* **2017**, *7*, 1700005. [[CrossRef](#)]
36. Pan, X.Y.; Yang, M.Q.; Fu, X.Z.; Zhang, N.; Xu, Y.J. Defective TiO₂ with oxygen vacancies: Synthesis, properties and photocatalytic applications. *Nanoscale* **2013**, *5*, 3601–3614. [[CrossRef](#)]
37. Li, Y.; Qian, J.; Zhang, M.H.; Wang, S.; Wang, Z.H.; Li, M.S.; Bai, Y.; An, Q.Y.; Xu, H.J.; Wu, F. Co-construction of sulfur vacancies and heterojunctions in tungsten disulfide to induce fast electronic/ionic diffusion kinetics for sodium-ion batteries. *Adv. Mater.* **2020**, *32*, 2005802. [[CrossRef](#)]
38. Yao, W.Q.; Tian, C.H.; Yang, C.; Xu, J.; Meng, Y.F.; Manke, I.; Chen, N.; Wu, Z.L.; Zhan, L.; Wang, Y.L.; et al. P-doped NiTe₂ with Te-vacancies in lithium-sulfur batteries prevents shuttling and promotes polysulfide conversion. *Adv. Mater.* **2022**, *34*, 2106370. [[CrossRef](#)]
39. Zhao, M.; Li, S.L.; Wu, X.; Luo, S.H. Gallium ion pre-insertion protocol to (NH₄)₂V₁₀O₂₅·8H₂O cathode materials for reversible aqueous Zn battery. *Adv. Mater. Technol.* **2024**, *9*, 2400125. [[CrossRef](#)]
40. Liu, W.; Su, Q.M.; Zhu, R.R.; Shi, W.H.; Zhang, F.; Du, G.H.; Zhao, W.Q.; Zhao, M.; Xu, B.S. Chemical lithiation-induced oxygen vacancies in MnO₂ at room temperature for aqueous zinc-ion batteries. *ACS Appl. Energy Mater.* **2023**, *6*, 6689–6699. [[CrossRef](#)]
41. Yang, J.; Xiao, X.; Chen, P.; Zhu, K.; Cheng, K.; Ye, K.; Wang, G.L.; Cao, D.X.; Yan, J. Creating oxygen-vacancies in MoO_{3-x} nanobelts toward high volumetric energy-density asymmetric supercapacitors with long lifespan. *Nano Energy* **2019**, *58*, 455–465. [[CrossRef](#)]
42. Zhang, Y.Y.; Chen, P.; Wang, Q.Y.; Wang, Q.; Zhu, K.; Ye, K.; Wang, G.L.; Cao, D.X.; Yan, J.; Zhang, Q. High capacity and kinetically accelerated lithium storage in MoO₃ enabled by oxygen vacancies and heterostructure. *Adv. Energy Mater.* **2021**, *11*, 2101712. [[CrossRef](#)]
43. Zhai, X.Z.; Qu, J.; Hao, S.M.; Jing, Y.Q.; Chang, W.; Wang, J.; Li, W.; Abdelkrim, Y.; Yuan, H.F.; Yu, Z.Z. Layered birnessite cathode with a displacement/intercalation mechanism for high-performance aqueous zinc-ion batteries. *Nano-Micro Lett.* **2020**, *12*, 56. [[CrossRef](#)] [[PubMed](#)]
44. Lu, Y.Q.; Deng, H.; Pan, T.T.; Zhang, C.B.; He, H. Thermal annealing induced surface oxygen vacancy clusters in α-MnO₂ nanowires for catalytic ozonation of VOCs at ambient temperature. *ACS Appl. Mater. Interfaces* **2023**, *15*, 9362–9372. [[CrossRef](#)]

45. Zhang, J.; He, T.; Zhang, W.; Sheng, J.Z.; Amiinu, I.S.; Kou, Z.K.; Yang, J.L.; Mai, L.Q.; Mu, S.C. Na Mn-O nanocrystals as a high capacity and long-life anode material for Li-ion batteries. *Adv. Energy Mater.* **2017**, *7*, 1602092. [[CrossRef](#)]
46. Wang, S.; Li, L.; He, W.; Shao, Y.; Li, Y. Oxygen vacancy modulation of bimetallic oxynitride anodes toward advanced Li-ion capacitors. *Adv. Funct. Mater.* **2020**, *30*, 2000350. [[CrossRef](#)]
47. Zhang, Z.C.Y.; Xi, B.J.; Wang, X.; Ma, X.J.; Chen, W.H.; Feng, J.K.; Xiong, S.L. Oxygen defects engineering of $\text{VO}_2 \cdot \text{xH}_2\text{O}$ nanosheets via in situ polypyrrole polymerization for efficient aqueous zinc ion storage. *Adv. Funct. Mater.* **2021**, *31*, 2103070. [[CrossRef](#)]
48. Alfaruqi, M.H.; Mathew, V.; Gim, J.; Kim, S.; Song, J.; Baboo, J.P.; Choi, S.H.; Kim, J. Electrochemically induced structural transformation in a $\gamma\text{-MnO}_2$ cathode of a high capacity zinc-ion battery system. *Chem. Mater.* **2015**, *27*, 3609–3620. [[CrossRef](#)]
49. Guo, C.; Zhou, Q.H.; Liu, H.M.; Tian, S.; Chen, B.L.; Zhao, J.; Li, J.F. A case study of β -and $\delta\text{-MnO}_2$ with different crystallographic forms on ion-storage in rechargeable aqueous zinc ion battery. *Electrochim. Acta* **2019**, *324*, 134867. [[CrossRef](#)]
50. Liu, Y.; Wu, X. Hydrogen and sodium ions Co-intercalated vanadium dioxide electrode materials with enhanced zinc ion storage capacity. *Nano Energy* **2021**, *86*, 106124. [[CrossRef](#)]
51. Bai, Y.C.; Zhang, H.; Xiang, B.; Yao, Q.; Dou, L.; Dong, G.Y. Engineering porous structure in Bi-component-active ZnO quantum dots anchored vanadium nitride boost's reaction kinetics for zinc storage. *Nano Energy* **2021**, *89*, 106386. [[CrossRef](#)]
52. Xiong, T.; Yu, Z.G.; Wu, H.J.; Du, Y.H.; Xie, Q.D.; Chen, J.S.; Xue, J.M. Defect engineering of oxygen-deficient manganese oxide to achieve high-performing aqueous zinc ion battery. *Adv. Energy Mater.* **2019**, *9*, 1803815. [[CrossRef](#)]
53. Li, N.; Hou, Z.D.; Liang, S.Y.; Cao, Y.J.; Liu, H.Y.; Hua, W.; Wei, C.G.; Kang, F.Y.; Wang, J.G. Highly flexible MnO_2 @polyaniline core-shell nanowire film toward substantially expedited zinc energy storage. *Chem. Eng. J.* **2023**, *452*, 139408. [[CrossRef](#)]
54. Xie, Q.X.; Cheng, G.; Xue, T.; Huang, L.H.; Chen, S.H.; Sun, Y.; Sun, M.; Wang, H.Z.; Yu, L. Alkali ions pre-intercalation of $\delta\text{-MnO}_2$ nanosheets for high-capacity and stable Zn-ion battery. *Mater. Today Energy* **2022**, *24*, 100934. [[CrossRef](#)]
55. Zhao, Y.J.; Zhang, P.J.; Liang, J.R.; Xia, X.Y.; Ren, L.T.; Li, S.; Liu, W.; Sun, X.M. Uncovering sulfur doping effect in MnO_2 nanosheets as an efficient cathode for aqueous zinc ion battery. *Energy Storage Mater.* **2022**, *47*, 424–433. [[CrossRef](#)]
56. Alfaruqi, M.H.; Islam, S.; Mathew, V.; Song, J.; Kim, S.; Tung, D.P.; Kim, J. Ambient redox synthesis of vanadium-doped manganese dioxide nanoparticles and their enhanced zinc storage properties. *Appl. Surf. Sci.* **2017**, *404*, 435–442. [[CrossRef](#)]
57. Tang, H.; Chen, W.H.; Li, N.; Hu, Z.L.; Xiao, L.; Xie, Y.J.; Xi, L.J.; Ni, L.; Zhu, Y.R. Layered MnO_2 nanodots as high-rate and stable cathode materials for aqueous zinc-ion storage. *Energy Storage Mater.* **2022**, *48*, 335–343. [[CrossRef](#)]
58. Zhao, C.R.; Liu, Y.; Li, S.L.; Wu, X.; Liu, J.H. PVP decorated $\text{H}_{3.78}\text{V}_6\text{O}_{13}$ microspheres assembled by nanosheets for aqueous zinc ion batteries at variable work temperature. *Chinese Chem. Lett.* **2024**, *2024*, 110185. [[CrossRef](#)]
59. Liu, S.C.; Zhu, H.; Zhang, B.H.; Zhu, H.K.; Ren, Y.; Geng, H.B.; Li, Q.; Li, C.C. Tuning the kinetics of zinc-ion insertion/extraction in V_2O_5 by in situ polyaniline intercalation enables improved aqueous zinc-ion storage performance. *Adv. Mater.* **2020**, *32*, 2001113. [[CrossRef](#)]
60. Yang, X.; Deng, W.Z.; Chen, M.; Wang, Y.B.; Sun, C.F. Mass-producible, quasi-zero-strain, lattice-water-rich inorganic open frameworks for ultrafast-charging and long-cycling zinc-ion batteries. *Adv. Mater.* **2020**, *32*, 2003592. [[CrossRef](#)]
61. Yang, S.H.; Zhang, L.; Luo, M.J.; Cui, Y.W.; Wang, J.Q.; Zhao, D.G.; Yang, C.; Wang, X.T.; Cao, B.Q. Synergistic combination of a Co-doped $\sigma\text{-MnO}_2$ cathode with an electrolyte additive for a high-performance aqueous zinc-ion battery. *ChemPhysMater* **2023**, *2*, 77–82. [[CrossRef](#)]
62. Liu, F.; Chen, Z.X.; Fang, G.Z.; Wang, Z.Q.; Cai, Y.S.; Tang, B.Y.; Zhou, J.; Liang, S.Q. V_2O_5 nanospheres with mixed vanadium valences as high electrochemically active aqueous zinc-ion battery cathode. *Nano-Micro Lett.* **2019**, *11*, 25. [[CrossRef](#)] [[PubMed](#)]
63. Xu, J.W.; Gao, Q.L.; Xia, Y.M.; Lin, X.S.; Liu, W.L.; Ren, M.M.; Kong, F.G.; Wang, S.J.; Lin, C. High-performance reversible aqueous zinc-ion battery based on iron-doped alpha-manganese dioxide coated by polypyrrole. *J. Colloid Interface Sci.* **2021**, *598*, 419–429. [[CrossRef](#)] [[PubMed](#)]

Disclaimer/Publisher’s Note: The statements, opinions and data contained in all publications are solely those of the individual author(s) and contributor(s) and not of MDPI and/or the editor(s). MDPI and/or the editor(s) disclaim responsibility for any injury to people or property resulting from any ideas, methods, instructions or products referred to in the content.